# Electric-field-induced epitaxial breakdown and emergent magnetoresistance due to strong oxygen reduction in Ca-doped $BiFeO_3$

Heung-Sik Park [1,2,*] Ji Soo Lim,[1,2,*] Jeonghun Suh,[1,2] and Chan-Ho Yang [1,2,3,†]

[1]*Department of Physics, Korea Advanced Institute of Science and Technology, Daejeon 34141, Republic of Korea*

[2]*Center for Lattice Defectronics, Korea Advanced Institute of Science and Technology, Daejeon 34141, Republic of Korea*

[3]*KAIST Institute for the NanoCentury, Korea Advanced Institute of Science and Technology, Daejeon 34141, Republic of Korea*

(Received 30 March 2021; accepted 14 January 2022; published 14 February 2022)

We study the structural and transport properties of a heavily oxygen-reduced region that is formed by electrical injection of a large amount of oxygen vacancies into a $Bi_{0.7}Ca_{0.3}FeO_{3-\delta}$ thin film. In electroforming, the epitaxial as-grown state is transformed into a disordered, polycrystalline phase. Nonohmic current-voltage relations, which can be interpreted as a space-charge-limited conduction, appear at low temperatures. As temperature increases, the curvature of the current-voltage relationship gradually changes to be nearly ohmic at and above 100 K. The maximum value of magnetoresistance, as large as $-2.6\%$ at 90 kOe, is attained at the same temperature of $\sim$100 K, which is significantly larger than $-0.1\%$ at 25 K and $-1.3\%$ at 300 K.

DOI: 10.1103/PhysRevMaterials.6.024404

## I. INTRODUCTION

Oxygen vacancies are omnipresent in oxides and provide opportunities into intriguing phenomena such as superconductivity [1], magnetoresistance [2], and ferroelectricity [3]. Various technological applications have exploited either the migration of oxygen vacancies or the resulting change in the material properties, such as in batteries [4], solid oxide fuel cells [5], resistive switching memories [6,7], and sensors [8]. The electroforming process provides a powerful way to manipulate oxygen vacancy concentration through the use of an electrical bias for migrating charged ions. Even a thermodynamically stable phase, which is barely oxidized under 100 atm of $O_2$ at 800 °C [9], can be electrically oxidized at low temperatures ($T$). Thus, this process can create highly oxidized or reduced phases, which are hardly obtained by conventional annealing methods [10]. Electroforming experiments are usually conducted on the conventional parallel-capacitor geometry with top and bottom electrodes, particularly in studies of resistive switching memory [11,12] and dielectrics [13]. However, by using an apparatus featuring a lateral device with coplanar electrodes relatively far apart from each other (a few hundred micron), the electroformed phases in between are spatially separated wide enough to perform selective measurements of physical properties from a particular phase. Furthermore, this method employing optical microscopy enables observations of electroforming in real time. The visualization in conjunction with postquantification analysis offers an efficient pathway to observe various dynamic behaviors such as filamentary conduction propagation [14] and turbulence [15].

Ca-doped $BiFeO_3$ ($Bi_{0.7}Ca_{0.3}FeO_{3-\delta}$) (BCFO) shows resistive switching phenomena [16], high ionic mobility [15], and electrochromism [17]. The 30% Ca-ion substitution into Bi sites makes the material tetragonal. By separating from the rhombohedral ferroelectric phase of pure and low (less than 15%) Ca-substituted $BiFeO_3$ [16], we can pay attention to the inherent ionic migration property avoiding the involvement of complex ferroelectric domain textures and defect dipole problems. Moreover, the compound contains sufficiently high oxygen vacancies, as much as $\delta \sim 0.15$ [10]. Additionally, various electroforming experiments have been previously conducted in BCFO thin films utilizing lateral devices with coplanar electrodes [10,14,15], generating a nonuniform distribution of oxygen vacancies in a quasiclosed oxygen system. As a result, three competing states arise: the as-grown phase, oxidized phase, and the oxygen-reduction phase. In the as-grown phase, the balanced coexistence of oxygen-vacancy donors and Ca ion acceptors cancel their electronic carriers leading to a compensated semiconductor with a yellowish semitransparent color [10,15]. The previous works have mainly focused on the as-grown and oxidized phases, and their boundary. Here, we characterize the oxygen-reduction region where oxygen vacancies are highly confined in a narrow region near the cathode, and explore the possibility of emergent conduction properties in the so far unexplored heavily $n$-type doping regime of $BiFeO_3$. These efforts not only provide useful insights into the electrochemical reactions of solids, but also provide an alternative route to the electrical formation of highly oxygen-reducing phases such as nickelate superconductors [1].

## II. SAMPLE PREPARATION

A BCFO thin film was deposited on a $SrTiO_3$ (100) substrate (CrysTec GmbH) by pulsed laser deposition. The detailed growth condition was previously reported [15]. The

*These authors contributed equally to this work.

†chyang@kaist.ac.kr

 

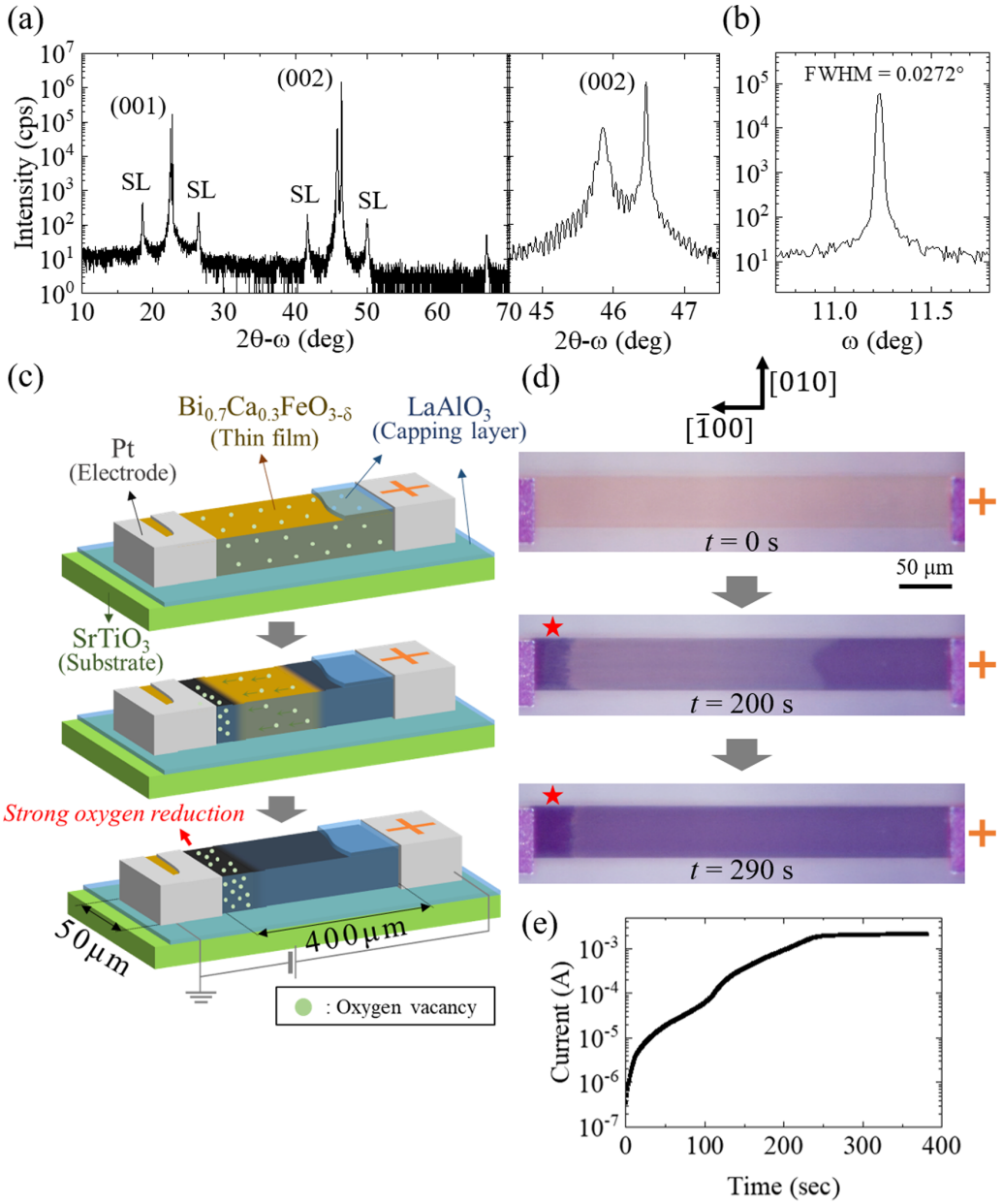


FIG. 1. X-ray diffraction of the as-grown Ca-doped $BiFeO_3$ ($Bi_{0.7}Ca_{0.3}FeO_{3-\delta}$) (BCFO) thin film and scheme of the experiment. (a) $2\theta$-$\omega$ plot of the as-grown BCFO thin film. Peaks at "SL" originate from the ordering of oxygen vacancies. The rightmost inset enlarges the curve near (002). (b) $\omega$ rocking curve. (c) Schematic of electroforming in the coplanar device for generating the oxygen-vacancy-rich phase. Circles qualitatively describe the concentration of oxygen vacancies in each phase. (d) Optical microscopy images of the device, showing the evolution of electroforming with time $t$. The red asterisks indicate the oxygen-reduction regions. The directions of polarizer and analyzer of the optical microscope were set to be perpendicular to each other. (e) Real-time channel current monitored as a function of $V$ application time.

epitaxial BCFO thin film (∼100 nm in thickness) with Ca 30% substitution was grown. X-ray diffraction characterizations show the sample has superlattice peaks due to 5-unit-cell modulation of pseudocubic cells along the $c$ axis as a consequence of oxygen vacancy ordering [Fig. 1(a)] [18] and small mosaicity is observed in the $\omega$-rocking curve [Fig. 1(b)]. A lateral channel device with coplanar electrodes was fabricated for electroforming experiments as follows. A 400-$\mu$m-long and 50-$\mu$m-wide bar-shaped sample was made with ultraviolet lithography and argon ion milling. We note that a transparent $LaAlO_3$ capping layer (10 nm thick) was *ex situ* deposited on the patterned BCFO channel by pulsed laser deposition at a growth $T$ of 650 °C with an oxygen partial pressure of 1 mTorr, as $LaAlO_3$ has a high defect formation energy, greater than 7 eV [19,20], and thus, can prevent the BCFO film from reacting with the atmosphere. Therefore, with regard to oxygen ions, the channel of a BCFO film is considered a quasi-isolated system. Pt metal was deposited as coplanar electrodes on both sides of the bar-shaped sample just after *in situ* milling the capping layer on the defined electrode areas, because Pt and BCFO form almost no Schottky barriers, and thus, the contacts are nearly ohmic for the pristine and oxidized phases with $p$-type carriers [21]. The entire fabrication processes are depicted in Figs. S1(a)–S1(g) of the

Supplemental Material [22]. For creating a nonuniform configuration of oxygen vacancy distribution, 25 V was applied between the coplanar electrodes at 300 °C in ambient conditions [Fig. 1(c)]. Thereafter, two kinds of visibly dark phases appeared on both sides of the sample due to the migration of oxygen vacancies at high $T$. Over time, the two dark phases expanded to fill the nearly entire sample except for the narrow depletion region at the interface. The dark phase on the side of a positively biased electrode covering a majority of area is the hole-doped ($p$-type) phase, because the electric field removed positively charged ionized oxygen vacancies that played a role of double electron donors, as confirmed by x-ray photoelectron spectroscopy, indicating that almost all the oxygen vacancies were removed [10]. Meanwhile, the removed oxygen vacancies were accumulated near the ground electrode. Provided that the total amount of oxygen ions is conserved due to the capping layer, the density of oxygen vacancies would be high in the resulting narrow region. The optical microscope images in Fig. 1(d) show the evolution of an electroforming channel with the region with high oxygen-vacancy density indicated by red asterisks. On the naïve assumption that the relative ratio of the oxygen-reduction area to the $p$-type area is ∼10% and the BCFO channel encapsulated by oxygen barrier is a closed system, we estimate the oxygen vacancy concentration $\delta$ to be close to 1.5 in the oxygen-vacancy confined region. It is a considerably large amount, enough to deteriorate the crystal structure and change the valence state. A pale dark color of the central region at $t = 200$ s is attributed to the existence of an intermediate state, which can have dark filaments imbedded in the dark-yellow intermediate phase [14].

Figure 1(e) shows the real-time channel current recorded during the electroforming. The current increased by four orders of magnitude and was saturated to a level of ∼2 mA after a forming time of ∼240 s. Simultaneously, the color contrast profile did not change appreciably after the forming time and remained similar to the image taken at 290 s. The constant current after the electroforming time suggests that the ion distribution reaches a steady state under bias and the change in $T$ through Joule heating is negligible.

## III. ATOMIC-SCALE STRUCTURE

To reveal atomic-scale configuration of the oxygen-reduction region, we performed high-angle annular dark-field (HAADF) scanning transmission electron microscopy (STEM) using a Titan cubed G2 60–300 (FEI Company) operating at an acceleration voltage of 200 kV for a specimen prepared by ultrahigh resolution focused ion beam (Helios G4) with an in-plane [100] zone axis. In contrast to the well-ordered epitaxial structure in the as-grown phase as shown in the x-ray diffraction results in Figs. 1(a) and 1(b), this region shows a coarse-grained texture [Fig. 2(a)]. The resulting disorder can be easily identified by comparing its crystallinity with those of the capping layer $LaAlO_3$ and the underlying substrate $SrTiO_3$ shown in the same image. The BCFO grains are of a nanometer-sized shape and crystal orientations seem to be aligned primarily along the original axes [Fig. 2(b)]. Figure 2(c) shows the fast Fourier transform result of the STEM image in Fig. 2(b), indicating not only the presence of a

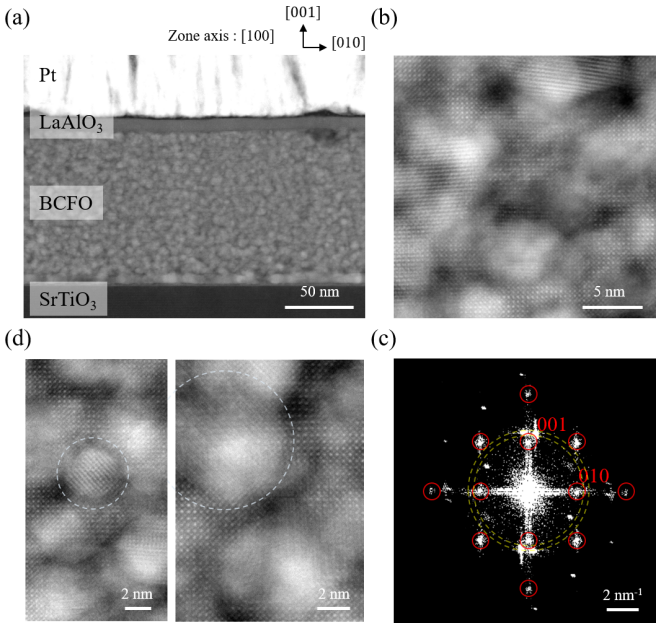


FIG. 2. STEM images of the oxygen-reduction region of BCFO. (a) Low magnification HAADF image. (b) High magnification HAADF image. (c) Diffraction image obtained by fast Fourier transform for (b), wherein red circles indicate diffraction spots of a perovskite structure and yellow dashed circles indicate unidentified second phase. (d) Nanoparticles of a circular shape with several nanometer sizes are notable.

perovskite structure with a lattice parameter of $c = \sim 0.39$ nm (red solid circles), but the diffraction spots at $d = \sim 0.32$ nm arising from an unidentified second phase are also observed (yellow dashed circles) (see Fig. S2 of [22] for a detailed analysis). In some areas, circular grains with a diameter of a few nanometers are observed [Fig. 2(d)]. The lattice parameters of ∼0.39 nm calculated from the perovskite regions are consistent with those of as-grown phase of BCFO on a $SrTiO_3$ (100) substrate [16]. Epitaxial breakdown occurs from the fully coherent epitaxial film to a granular film with significant ion substitution and change, but the original structure and orientation seem to remain in most areas of the oxygen-reduction region.

Figure 3 shows electron energy loss spectroscopy (EELS) results of the brighter and darker regions from the annular dark-field image shown in Fig. 3(a). Figure 3(b) represents the electron energy loss spectra near the Fe $L$ edge for two representative positions. The background intensity was removed by interpolation of the spectra near the Fe $L_{2,3}$ edge. $L_3$ and $L_2$ peaks of both spectra are fitted to Lorentzian function (blue dashed lines). $L_3/L_2$ intensity ratio obtained from the height of each Lorentzian functions is 4.56 for the brighter region and 5.07 for the darker region. According to the work of Cavé *et al.*, the iron valence ratio ($Fe^{3+}/\Sigma Fe$), which represents the relative fraction of $Fe^{3+}$ ions between ferrous ($Fe^{2+}$) and ferric ($Fe^{3+}$) valences, can be calculated from the relative ratio of Fe $L_3$ intensity to $L_2$ intensity in EELS measurements [23]. From the calibration model of $Fe^{3+}/\Sigma Fe$ versus $L_3/L_2$ ratio [23], the value of $Fe^{3+}/\Sigma Fe$ in our BCFO film can be estimated as 0.36 (0.70) for the brighter (darker) region.

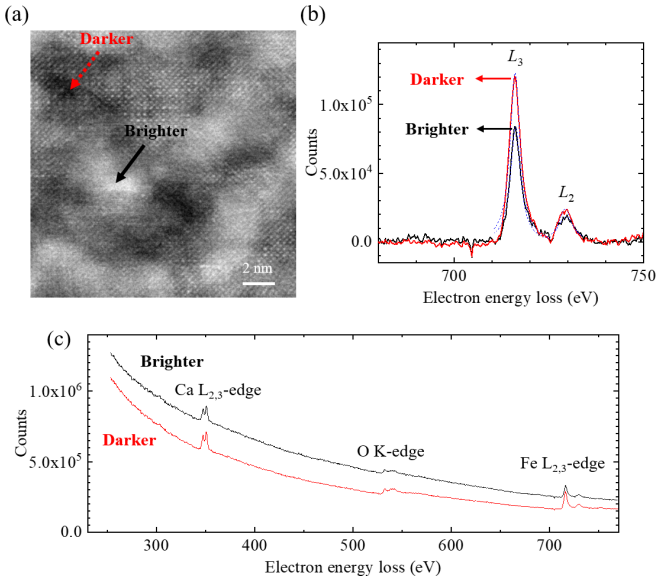


FIG. 3. EELS study of an oxygen-reduction area of BCFO. (a) Incident beam positions at a bright position (indicated by a black solid arrow), and a darker position (indicated by a red dotted arrow). (b) EELS spectra near the Fe $L$ edges for the positions. Blue dashed curves are Lorentzian curves fitted to the peaks. (c) EELS spectra for a wide range of energy loss, which include Ca $L$-edge, O $K$-edge, and Fe $L$-edge peaks.

Considering that magnetite ($Fe_3O_4$ or $Fe^{2+}Fe_2{}^{3+}O_4$) has a $Fe^{3+}/\Sigma Fe$ value of 0.67, the darker areas have a valence state similar to $Fe_3O_4$, and that of the brighter areas decrease more, closer to $Fe^{2+}$. However, as shown in the EELS spectra for a wide range of energy loss in Fig. 3(c), the Ca $L$-edge peaks are clearly detected. The oxygen-reduction phase contains Ca ions and thus it is compositionally distinct from $Fe_3O_4$. The lowering of Fe valence state is mainly driven by the introduction of oxygen vacancies.

## IV. ELECTRICAL TRANSPORT MEASUREMENTS

The electrical transport property of the oxygen-reduction BCFO state was measured using a commercial low-$T$ system (Quantum Design PPMS 9T) equipped with a current source (Keithley 6221), a high resistance meter (Keithley 6517A), and a multimeter (Keithley 2001). Figure 4(a) shows a schematic of the four electrodes deposited on the oxygen-reduction region. Note that the original Pt electrodes used for electroforming were removed and then we etched the $LaAlO_3$ capping layer on the areas where the additional four electrodes would be deposited [Figs. S1(h)–S1(j) of [22]]. Since the oxygen-reduction region and the oxidized region each have heavily more $n$-type and $p$-type carriers than the as-grown insulating phase, there should be a depletion region in between and the region appeared to be a more optically transparent strip. Thus, the oxygen-reduction region can be isolated from the oxidized region in terms of electrical connection.

A semiconducting behavior is observed above 75 K following a simple Arrhenius relation with an activation energy of 49 meV [Fig. 4(b)]. However, the behavior deviates from the Arrhenius relation below 75 K and the variation of resistance ($R$)

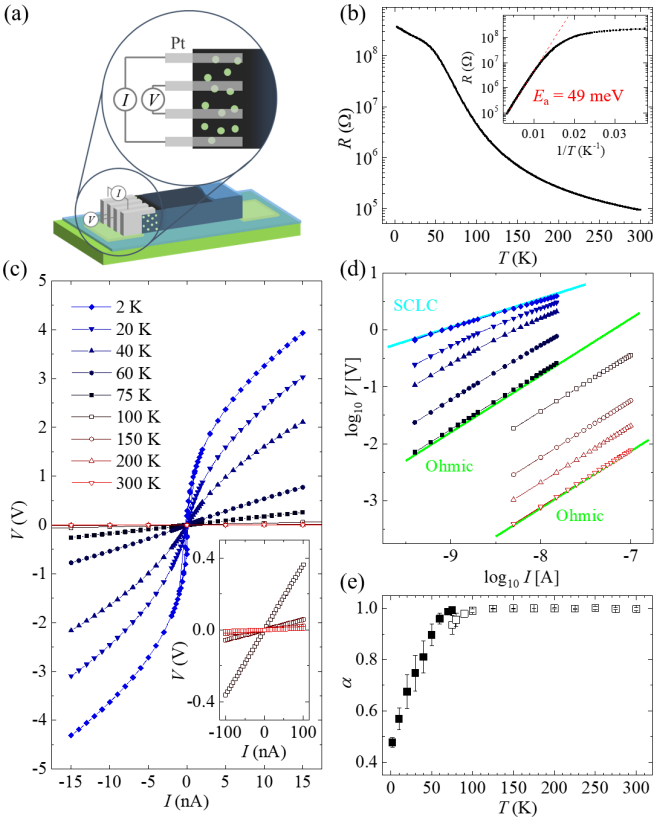


FIG. 4. Electrical transport properties of the oxygen-reduction region of BCFO. (a) A four-point probe is deposited on the oxygen-vacancy-rich phase after removal of the original Pt electrodes and the capping layer. (b) $R$-$T$ curve with inset showing resistance as a function of $T^{-1}$ and red dotted line representing Arrhenius relation with an activation energy of 49 meV. (c) $I$-$V$ curves measured up to 15 nA. Inset shows $I$-$V$ curves at 100–300 K up to 100 nA. (d) Double logarithmic plots of the $I$-$V$ curves in (c) with the guide lines representing SCLC and ohmic conduction. (e) Variation of slopes, $\alpha$, obtained from the linear regression ($\log_{10}V \sim \alpha \log_{10}I + \beta$) of (d) with respect to $T$. Data measured from 2 to 75 K are marked with solid squares, while results from 75 to 300 K are marked with open squares. Error bars represent 10 times of standard errors.

becomes gentler, suggesting the existence of a competing conduction mechanism. Isothermal current-voltage ($I$-$V$) curves were measured at selected $T$ ranging 2–300 K. In consideration of a large variation of $R$ depending on $T$, two $I$ levels were used: a constant $I$ of 15 nA was used for the $T$ range of 2–75 K and 100 nA for 100–300 K [Fig. 4(c)]. The measured $I$-$V$ curves indicate that nonohmic behavior occurs at far below 100 K and the ohmic behavior appears as $T$ approaches 75 K. At low $T$, the nonlinear $I$-$V$ curves can be better analyzed in double logarithmic plots [Fig. 4(d)]. In accordance with the linear regression, $\log_{10}V = \alpha \log_{10}I + \beta$, the power exponent $\alpha$ is plotted as a function of $T$ in Fig. 4(e). At low $T$, $\alpha$ is near 0.5, indicating that $I$ is proportional to $V^2$, suggesting that space-charge limited current (SCLC) is the dominant transport mechanism at low $T$ [24]. Near 75 K, $\alpha$ becomes unity ($I$ is linearly proportional to $V$), and therefore, ohmic conduction is dominant in the intermediate and high $T$ ranges. One possibility for this change in the primary conduction mechanism

is the conversion of charge carriers from injected carriers to thermally generated carriers. At 2 K, charge carriers injected from the electrode constitute space charges, and thus, SCLC becomes the primary conduction mechanism. As $T$ increases to 10–50 K, ohmic behavior due to thermally generated carriers begins to arise at weak injection ($V < 0.3$ V). At stronger injection ($V > 0.3$ V) trap-limited SCLC arises. That is the reason why the $I$-$V$ curves on the double logarithmic plot at 10–50 K are not perfectly fitted with the linear regression. Thus, $\alpha$ values in this $T$ range have no direct meaning but it qualitatively describes that a crossover of the SCLC and ohmic conductions occurs within the $I$ range. In general, an $I$-$V$ curve of the SCLC has four regimes. As described above, ohmic conduction changes to the trap-limited SCLC with quadratic $V$ dependence as $I$ increases. In the third regime, $I$ can increase abruptly when $V$ reaches the trap-filled-limit voltage. In the fourth regime, trap-free SCLC, the abrupt current increase ceases and the quadratic $V$ dependency resumes. Therefore, considering that no abrupt increase in $I$ was observed, we realize that the conduction does not reach the third and fourth regimes, but remains within the second regime of SCLC in our measurements. The diffusion $I$ can be ignored compared to the field-driven drift $I$ at sufficiently low $k_B T \ll eV$. Accordingly, the Mott-Gurney law can be used for describing the trap-limited SCLC. Thus, $I$ can be written as a sum of the ohmic conduction and the trap-limited SCLC,

$$I = ne\mu\frac{A}{s}V + \frac{9\mu k\varepsilon_0 A}{8s^3}\frac{n}{n_t}V^2, \tag{1}$$

where $n$, $e$, and $\mu$ stand for the density, charge, and mobility of free electronic carriers. $A$ and $s$ are the area and length of the BCFO channel, $k$ is the dielectric constant, $\epsilon_0$ is the vacuum permittivity, and $n_t$ is the trapped charge density. The crossover voltage ($V_{cr}$) between those two conduction mechanisms can be deduced by equalizing the first and second terms of Eq. (1),

$$ne\mu\frac{A}{s}V_{cr} = \frac{9\mu k\varepsilon_0 A}{8s^3}\frac{n}{n_t}V_{cr}^2. \tag{2}$$

Thus, $V_{cr}$ can be expressed as

$$V_{cr} = \left(\frac{8es^2}{9}\right)\frac{n_t}{k\varepsilon_0}. \tag{3}$$

Measuring $V_{cr}$ determines the ratio of the trapped charge density to the dielectric constant. The $I$-$V$ curves at low $T$ in Fig. 4(d) show that $V_{cr}$ is approximately 0.3 V, indicating $n_t/k\varepsilon_0 \sim 10^{28}$ V C$^{-1}$ m$^{-2}$. Assuming $k \sim 100$ for an order estimation, the value of $n_t$ can be estimated as $10^{13}$ cm$^{-3}$. At 75 K, thermally generated delocalized carriers begin to dominate overall conduction, showing ohmic behavior.

Figure 5 shows the magnetoresistance ($MR$) measurements of the oxygen-reduction phase of BCFO. Magnetic fields up to 90 kOe were applied perpendicular to the thin film. A DC bias $I$ of 15 nA was used at 25–75 K, whereas AC $I$ at 1.3 Hz was used in the range 100–300 K to employ lock-in technique for reducing noise at high $T$. Figure 5(a) shows the ratio of $R$ changes by magnetic field in percent, defined as $MR(\%) = [R(B)–R(0)]/R(0) \times 100$, at selected values of $T$. Remarkably, large negative $MR$ of a few % emerges, suggesting that the oxygen-reduction phase has magnetic ordering

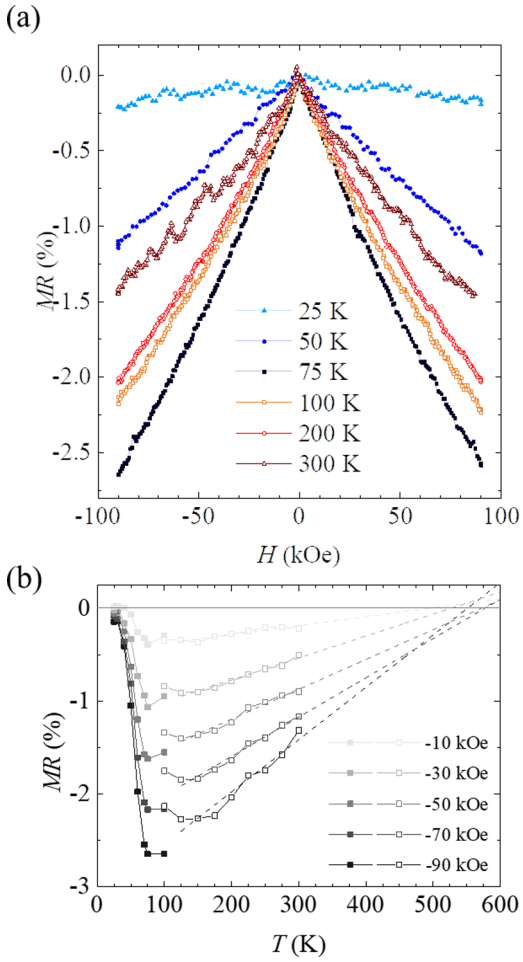


FIG. 5. Negative $MR$ of the oxygen-reduction region of BCFO. (a) $MR$ measured under DC $I$ 15 nA (for 25, 50, 75 K) and under AC $I$ at 1.3 Hz with various amplitudes (20 nA for 100 K, 100 nA for 200 K, 100 nA for 300 K). (b) Plot of $MR$ as a function of $T$. Measurements performed with DC $I$ are marked with solid squares while measurements with AC $I$ are marked with open squares. Dashed lines extrapolate $MR$ above 100 K.

due to the significant mixture of $Fe^{3+}$ and $Fe^{2+}$ valence states. Negative $MR$ (%) at $H = -10, -30, -50, -70, -90$ kOe are plotted in Fig. 5(b). The low-$T$ data measured with DC $I$ are marked by solid squares, while high-$T$ results with AC $I$ are indicated by open squares. The noticeable mismatch between the solid and open symbols is thought to arise from a slow aging effect in a glassy magnetic state in external magnetic fields. The high $T$ (open symbols) data with cooling were acquired earlier than the low $T$ (solid symbols) data. The magnitude of $MR$ abruptly increases as $T$ increases from 25 to 100 K. A maximum negative $MR$ of $-2.6\%$ is observed near 100 K. The value then steadily decreases to $-1.3\%$ at 300 K.

Considering that the negative $MR$ from disordered magnetic moments at grain boundaries [25,26], a large density of grain boundaries in our sample with similar Fe valence states may cause the similar magnetotransport behaviors. It is another picture that magnetic BCFO nanoparticles behave as if they possess superparamagnetic spins and their magnetic frustration makes a glassy state [27]. It is worth mentioning

that the *MR* curves from different magnetic fields extrapolate to zero at similar $T$ ranges, 500–580 K, indicating the spin glass transition $T$. Although we investigated effects of field or zero-fieldcooling from 300 K on the *R-T* curve, we did not observe any systematic variation (see Fig. S3 of [22]). The appropriate field-cooling experiment from a higher $T$ than the spin glass $T$ is difficult to implement because the heating deteriorates the oxygen-reduction state.

## V. CONCLUSIONS

In this study, a heavily oxygen-reduction state of BCFO was prepared by electroforming using a lateral device with coplanar electrodes. Structural and transport properties of the oxygen-vacancy-rich BCFO region were examined. Intensive injection of oxygen vacancies induced an epitaxial breakdown leading to a polycrystalline structure with nanometer-sized grains. Nonohmic transport behavior is observed for $T$ below 100 K and the dominant conduction mechanism can be described by SCLC. Negative *MR* is maximized to be $-2.6\%$ at 100 K where ohmic conduction emerges. The *MR* values of several percent persist up to room $T$.

## ACKNOWLEDGMENTS

This work was supported by the National Research Foundation (NRF) Grants funded by the Korean Government via the Creative Research Initiative Center for Lattice Defectronics (Grant No. 2017R1A3B1023686) and the Center for Quantum Coherence in Condensed Matter (Grant No. 2016R1A5A1008184). STEM measurements were conducted at KAIST Analysis Center for Research Advancement.

[1] R. J. Cava, B. Batlogg, C. H. Chen, E. A. Rietman, S. M. Zahurak, and D. Werder, Oxygen stoichiometry, superconductivity, and normal-state properties of $YBa_2Cu_3O_{7-\delta}$, Nature (London) **329**, 423 (1987).

[2] C. Ritter, M. R. Ibarra, J. M. De Teresa, P. A. Algarabel, C. Marquina, J. Blasco, J. Garcia, S. Oseroff, and S.-W. Cheong, Influence of oxygen content on the structural, magnetotransport, and magnetic properties of $LaMnO_{3+\delta}$, Phys. Rev. B **56**, 8902 (1997).

[3] C. H. Park and D. J. Chadi, Microscopic study of oxygen-vacancy defects in ferroelectric perovskites, Phys. Rev. B **57**, R13961 (1998).

[4] J. T. Mefford, W. G. Hardin, S. Dai, K. P. Johnston, and K. J. Stevenson, Anion charge storage through oxygen intercalation in $LaMnO_3$ perovskite pseudocapacitor electrodes, Nat. Mater. **13**, 726 (2014).

[5] V. V. Kharton, F. M. B. Marques, and A. Atkinson, Transport properties of solid oxide electrolyte ceramics: A brief review, Solid State Ion. **174**, 135 (2004).

[6] J. S. Lee, S. Lee, and T. W. Noh, Resistive switching phenomena: A review of statistical physics approaches, Appl. Phys. Rev. **2**, 031303 (2015).

[7] R. Waser and M. Aono, Nanoionics-based resistive switching memories, Nat. Mater. **6**, 833 (2007).

[8] R. Ramamoorthy, P. K. Dutta, and S. A. Akbar, Oxygen sensors: Materials, methods, designs and applications, J. Mater. Sci. **38**, 4271 (2003).

[9] N. Masó and A. R. West, Electrical properties of Ca-doped $BiFeO_3$ ceramics: From *p*-type semiconduction to oxide-ion conduction, Chem. Mater. **24**, 2127 (2012).

[10] J. S. Lim, J. H. Lee, A. Ikeda-Ohno, T. Ohkochi, K.-S. Kim, J. Seidel, and C.-H. Yang, Electric-field-induced insulator to Coulomb glass transition via oxygen-vacancy migration in Ca-doped $BiFeO_3$, Phys. Rev. B **94**, 035123 (2016).

[11] T. You, N. Du, S. Slesazeck, T. Mikolajick, G. Li, D. Bürger, I. Skorupa, H. Stöcker, B. Abendroth, A. Beyer *et al.*, Bipolar electric-field enhanced trapping and detrapping of mobile donors in $BiFeO_3$ memristors, ACS Appl. Mater. Interfaces **6**, 19758 (2014).

[12] J. M. Luo, S. H. Chen, S. L. Bu, and J. P. Wen, Resistive switching and Schottky diode-like behaviors in $Pt/BiFeO_3/ITO$ devices, J. Alloys Compd. **601**, 100 (2014).

[13] H. D. Chen, K. R. Udayakumar, K. K. Li, C. J. Gaskey, and L. E. Cross, Dielectric breakdown strength in sol-gel derived PZT thick films, Integr. Ferroelectr. **15**, 89 (1997).

[14] H.-S. Park, J. S. Lim, J. Suh, and C.-H. Yang, Real-time observation of filamentary conduction pathways in Ca-doped $BiFeO_3$, Appl. Phys. Lett. **115**, 183901 (2019).

[15] J. S. Lim, J. H. Lee, H.-S. Park, R. Gao, T. Y. Koo, L. W. Martin, R. Ramesh, and C.-H. Yang, Ultrafast collective oxygen-vacancy flow in Ca-doped $BiFeO_3$, NPG Asia Mater. **10**, 943 (2018).

[16] C.-H. Yang, J. Seidel, S. Y. Kim, P. B. Rossen, P. Yu, M. Gajek, Y. H. Chu, L. W. Martin, M. B. Holcomb, Q. He *et al.*, Electric modulation of conduction in multiferroic Ca-doped $BiFeO_3$ films, Nat. Mater. **8**, 485 (2009).

[17] J. Seidel, W. Luo, S. J. Suresha, P.-K. Nguyen, A. S. Lee, S.-Y. Kim, C.-H. Yang, S. J. Pennycook, S. T. Pantelides, J. F. Scott *et al.*, Prominent electrochromism through vacancy-order melting in a complex oxide, Nat. Commun. **3**, 799 (2012).

[18] M. Campanini, R. Erni, C.-H. Yang, R. Ramesh, and M. D. Rossell, Periodic giant polarization gradients in doped $BiFeO_3$ thin films, Nano Lett. **18**, 717 (2018).

[19] J. D. Sayre, K. T. Delaney, and N. A. Spaldin, Interplay between strain and oxygen vacancies in lanthanum aluminate, arXiv:1202.1431 (2012).

[20] M. T. Curnan and J. R. Kitchin, Effects of concentration, crystal structure, magnetism, and electronic structure method on first-principles oxygen vacancy formation energy trends in perovskites, J. Phys. Chem. C **118**, 28776 (2014).

[21] N. Masó, H. Beltrán, M. Prades, E. Cordoncillo, and A. R. West, Field-enhanced bulk conductivity and resistive-switching in Ca-doped $BiFeO_3$ ceramics, Phys. Chem. Chem. Phys. **16**, 19408 (2014).

[22] See Supplemental Material at http://link.aps.org/supplemental/10.1103/PhysRevMaterials.6.024404 for the detailed device fabrication procedure, HAADF images of secondary phases, and R-T curves after field cooling and zero-field cooling from 300 K.

[23] L. Cavé, T. Al, D. Loomer, S. Cogswell, and L. Weaver, A STEM/EELS method for mapping iron valence ratios in oxide minerals, Micron **37**, 301 (2006).

[24] L. Jin, H. Zhu, D. Chu, Y. Yang, C. Wang, N. Xie, Z. Huang, and J. Liu, Change in trap characteristics during fatigue of $Au/BiFeO_3/SrRuO_3$, Microelectron. Reliab. **108**, 113638 (2020).

[25] X. Liu, W. Mi, Q. Zhang, and X. Zhang, Magnetoresistance of epitaxial and polycrystalline $Fe_3O_4$ films near Verwey transition, Appl. Phys. Lett. **113**, 012401 (2018).

[26] W. B. Mi, J. J. Shen, E. Y. Jiang, and H. L. Bai, Microstructure, magnetic and magneto-transport properties of polycrystalline $Fe_3O_4$ films, Acta Mater. **55**, 1919 (2007).

[27] D. Peddis, D. Rinaldi, G. Ennas, A. Scano, E. Agostinelli, and D. Fiorani, Superparamagnetic blocking and superspin-glass freezing in ultra small $\delta$-$(Fe_{0.67}Mn_{0.33})OOH$ particles, Phys. Chem. Chem. Phys. **14**, 3162 (2012).